Navier-Stokes Calculations of Transonic Viscous Flow About Wing/Body Configurations

J. E. Deese* and R. K. Agarwal†
McDonnell Douglas Research Laboratories, St. Louis, Missouri

A three-dimensional Navier-Stokes solver has been developed for viscous transonic flow about transport and fighter wing/body configurations. The thin- and slender-layer approximations to the unsteady compressible Reynolds-averaged Navier-Stokes equations are solved by an explicit multistage Runge-Kutta method using a finite-volume formulation on body-conforming curvilinear grids. Efficiency is enhanced by employing local time stepping and vectorization. Microtasking enables the code to make optimal use of multiple processors. Comparisons of computed surface pressure distributions with experimental data for typical transport and fighter configurations show that the Navier-Stokes solutions improve prediction of shock strength and location over simpler Euler equation models.

Introduction

COMPUTATIONAL fluid dynamics has an increasingly important role in the design and analysis of aircraft as computer hardware becomes faster and algorithms become more efficient. Progress is being made in two directions: more complex and realistic configurations are being treated and algorithms based on higher approximations to the complete Navier-Stokes equations are being developed. The obvious goal is the solution of complete aircraft flowfields with the full Navier-Stokes equations.

The literature indicates that linear panel methods can model detailed realistic aircraft geometries in flow regimes where this approximation is valid. Solutions for nonlinear potential equations for flowfields about nearly complete aircraft configurations also have been available for some time. Recently, Euler methods have progressed to the point of computing flowfield solutions for complete aircraft.

As algorithms incorporating higher approximations to the Navier-Stokes equations are developed, computer resource requirements increase rapidly. Generation of suitable grids becomes more difficult and the number of grid points required to resolve flow features of interest increases. Coupling greater grid density with the greater execution time per point needed to solve more complex equations requires large computer memory and long run time. As a result, early work with the Navier-Stokes equations dealt with one- and two-dimensional flows or three-dimensional flow about simple geometries.

Recently, the development of large vector computers has enabled researchers to attempt modeling of more complex geometries with Navier-Stokes algorithms. Transonic-wing calculations have been reported by Agarwal and Deese,[1,2] Vatsa,[3] Holst et al.,[4] Vadyak,[5] and Thomas and Walters,[6] among others. Shang and Scheer[7] calculated the flowfield about a lifting-body aircraft and Flores et al.[8] have computed the flow about a fighter wing/body configuration.

In the present paper, the authors extend the method outlined in Ref. 2 to solve the Navier-Stokes equations for flowfields about transport and fighter wing/body configurations. A code has been developed which can compute flowfields using the Euler, thin- or slender-layer approximations to the governing equations.

The thin-layer approximation retains viscous terms in one direction. For turbulent flow with high Reynolds numbers, the dominant viscous effects are the result of diffusion normal to a body surface. The thin-layer approximation is then suitable for geometries where the body can be mapped onto a single plane in the computational space, retaining viscous terms normal to this plane. A typical example would be an isolated wing or fuselage.

The slender-layer approximation retains viscous terms in two directions, neglecting only streamwise terms. This approximation is useful for calculating viscous flows in regions where two aerodynamic surfaces interact, such as depicted by the shaded areas of Fig. 1. Viscous effects on both the fuselage and wing surfaces can be modeled with the slender-layer approximation.

The algorithm employed for solution of the equations is an explicit finite-volume time-stepping scheme. Spatial terms are central differenced and a combination of first- and third-order artificial dissipation is added to stabilize the method. Variable time steps are employed to speed convergence to steady state. Vectorization and microtasking have been applied to enhance efficiency and reduce wall clock time. Calculations for transport and fighter wing/body configurations are compared with experimental data.

Governing Equations

The governing equations are approximations to the full Reynolds-averaged, time-dependent, compressible Navier-Stokes equations in three dimensions for curvilinear coordinate systems. The slender-layer approximation will be outlined and appropriate modifications for the thin-layer and Euler approximations will be indicated.

Let p, ρ, (u,v,w), E, and H denote pressure, density, the three Cartesian velocity components, total energy, and total enthalpy, respectively. Define the effective viscosity as

$$\mu_{\text{eff}} = \mu_\ell + \mu_t \tag{1a}$$

and the effective thermal conductivity as

$$k_{\text{eff}} = k_\ell + k_t \tag{1b}$$

where μ_ℓ denotes the molecular viscosity, k_ℓ the conductivity, μ_t the turbulent eddy viscosity, and k_t the turbulent conductivity.

Let p_∞, ρ_∞, H_∞, μ_∞, and k_∞ denote the pressure, density, total enthalpy, molecular viscosity, and molecular thermal conductivity, respectively, in the freestream, and $\mathcal{L}$ be a typical body dimension in the flow. Various nondimensional variables

---

Presented as Paper 87-1200 at the AIAA 19th Fluid Dynamics, Plasma Dynamics, and Laser Conference, Honolulu, HI, June 8-10, 1987; received June 9, 1987; revision received June 17, 1988.

*Scientist. Member AIAA.

†Senior Scientist. Associate Fellow AIAA.

are defined as follows:

$$\bar{\rho} = \rho/\rho_\infty, \quad \bar{p} = p/p_\infty$$

$$(\bar{u},\bar{v},\bar{w}) = (u,v,w)/\sqrt{p_\infty/\rho_\infty}$$

$$\bar{E} = \rho_\infty(E - H_\infty)/p_\infty$$

$$\bar{H} = \rho_\infty(H - H_\infty)/p_\infty$$

$$\bar{\mu}_{\text{eff}} = \mu_{\text{eff}}/\mu_\infty$$

$$\bar{k}_{\text{eff}} = k_{\text{eff}}/k_\infty$$

$$(\bar{x},\bar{y},\bar{z}) = (x,y,z)/\mathcal{L}$$

$$\bar{t} = t/(\mathcal{L}\sqrt{\rho_\infty/p_\infty})$$

Let the functions $\xi = \xi(\bar{x},\bar{y},\bar{z})$, $\eta = \eta(\bar{x},\bar{y},\bar{z})$, and $\zeta = \zeta(\bar{x},\bar{y},\bar{z})$ describe the coordinate transformation between the Cartesian system $(\bar{x},\bar{y},\bar{z})$ and the body-oriented curvilinear system (ξ,η,ζ). For arbitrary geometric shapes, this transformation is accomplished numerically. The Jacobian J of the transformation and the associated derivatives are also obtained numerically.

In an arbitrary curvilinear coordinate system (ξ,η,ζ), the slender shear layer form of the Navier-Stokes equations is obtained as

$$\frac{\partial \hat{q}}{\partial \bar{t}} + \frac{\partial \hat{L}}{\partial \bar{\xi}} + \frac{\partial \hat{M}}{\partial \bar{\eta}} + \frac{\partial \hat{N}}{\partial \bar{\zeta}} = \frac{\sqrt{\gamma} M_\infty}{Re_\infty}(\hat{S}_1 + \hat{S}_2) \tag{2}$$

where

$$\hat{q} = qJ \tag{3a}$$

$$J = \bar{x}_\xi \bar{y}_\eta \bar{z}_\zeta + \bar{x}_\zeta \bar{y}_\xi \bar{z}_\eta + \bar{x}_\eta \bar{y}_\zeta \bar{z}_\xi - \bar{x}_\xi \bar{y}_\zeta \bar{z}_\eta - \bar{x}_\eta \bar{y}_\xi \bar{z}_\zeta - \bar{x}_\zeta \bar{y}_\eta \bar{z}_\xi \tag{3b}$$

$$\hat{L} = (\bar{y}_\eta \bar{z}_\zeta - \bar{y}_\zeta \bar{z}_\eta)L + (\bar{z}_\eta \bar{x}_\zeta - \bar{x}_\eta \bar{z}_\zeta)M + (\bar{x}_\eta \bar{y}_\zeta - \bar{y}_\eta \bar{x}_\zeta)N \tag{3c}$$

$$\hat{M} = (\bar{z}_\xi \bar{y}_\zeta - \bar{y}_\xi \bar{z}_\zeta)L + (\bar{x}_\xi \bar{z}_\zeta - \bar{x}_\zeta \bar{z}_\xi)M + (\bar{y}_\xi \bar{x}_\zeta - \bar{x}_\xi \bar{y}_\zeta)N \tag{3d}$$

$$\hat{N} = (\bar{y}_\xi \bar{z}_\eta - \bar{z}_\xi \bar{y}_\eta)L + (\bar{x}_\eta \bar{z}_\xi - \bar{x}_\xi \bar{z}_\eta)M + (\bar{x}_\xi \bar{y}_\eta - \bar{y}_\xi \bar{x}_\eta)N \tag{3e}$$

$$q = \begin{bmatrix} \bar{\rho} \\ \bar{\rho}\bar{u} \\ \bar{\rho}\bar{v} \\ \bar{\rho}\bar{w} \\ \bar{\rho}\bar{E} \end{bmatrix} \qquad L = \begin{bmatrix} \bar{\rho}\bar{u} \\ \bar{\rho}\bar{u}^2 + \bar{p} \\ \bar{\rho}\bar{u}\bar{v} \\ \bar{\rho}\bar{u}\bar{w} \\ \bar{\rho}\bar{u}\bar{H} \end{bmatrix}$$

$$M = \begin{bmatrix} \bar{\rho}\bar{v} \\ \bar{\rho}\bar{v}\bar{u} \\ \bar{\rho}\bar{v}^2 + \bar{p} \\ \bar{\rho}\bar{v}\bar{w} \\ \bar{\rho}\bar{v}\bar{H} \end{bmatrix} \qquad N = \begin{bmatrix} \bar{\rho}\bar{w} \\ \bar{\rho}\bar{w}\bar{u} \\ \bar{\rho}\bar{w}\bar{v} \\ \bar{\rho}\bar{w}^2 + \bar{p} \\ \bar{\rho}\bar{w}\bar{H} \end{bmatrix} \tag{3f}$$

$$\hat{S}_1 = \begin{bmatrix} 0 \\ (\bar{z}_\xi \bar{y}_\zeta - \bar{y}_\xi \bar{z}_\zeta)(n_{11})_\eta + (\bar{x}_\xi \bar{z}_\zeta - \bar{x}_\zeta \bar{z}_\xi)(n_{12})_\eta \\ \quad + (\bar{y}_\xi \bar{x}_\zeta - \bar{x}_\xi \bar{y}_\zeta)(n_{13})_\eta \\ (\bar{z}_\xi \bar{y}_\zeta - \bar{y}_\xi \bar{z}_\zeta)(n_{12})_\eta + (\bar{x}_\xi \bar{z}_\zeta - \bar{x}_\zeta \bar{z}_\xi)(n_{14})_\eta \\ \quad + (\bar{y}_\xi \bar{x}_\zeta - \bar{x}_\xi \bar{y}_\zeta)(n_{15})_\eta \\ (\bar{z}_\xi \bar{y}_\zeta - \bar{y}_\xi \bar{z}_\zeta)(n_{13})_\eta + (\bar{x}_\xi \bar{z}_\zeta - \bar{x}_\zeta \bar{z}_\xi)(n_{15})_\eta \\ \quad + (\bar{y}_\xi \bar{x}_\zeta - \bar{x}_\xi \bar{y}_\zeta)(n_{16})_\eta \\ (\bar{z}_\xi \bar{y}_\zeta - \bar{y}_\xi \bar{z}_\zeta)(\bar{u}n_{11} + \bar{v}n_{12} + \bar{w}n_{13} + n_{17})_\eta \\ \quad + (\bar{x}_\xi \bar{z}_\zeta - \bar{x}_\zeta \bar{z}_\xi)(\bar{u}n_{12} + \bar{v}n_{14} + \bar{w}n_{15} + n_{18})_\eta \\ \quad + (\bar{y}_\xi \bar{x}_\zeta - \bar{x}_\xi \bar{y}_\zeta)(\bar{u}n_{13} + \bar{v}n_{15} + \bar{w}n_{16} + n_{19})_\eta \end{bmatrix} \tag{3g}$$

$$\hat{S}_2 = \begin{bmatrix} 0 \\ (\bar{y}_\xi \bar{z}_\eta - \bar{z}_\xi \bar{y}_\eta)(n_{21})_\zeta + (\bar{x}_\eta \bar{z}_\xi - \bar{x}_\xi \bar{z}_\eta)(n_{22})_\zeta \\ \quad + (\bar{x}_\xi \bar{y}_\eta - \bar{y}_\xi \bar{x}_\eta)(n_{23})_\zeta \\ (\bar{y}_\xi \bar{z}_\eta - \bar{z}_\xi \bar{y}_\eta)(n_{22})_\zeta + (\bar{x}_\eta \bar{z}_\xi - \bar{x}_\xi \bar{z}_\eta)(n_{24})_\zeta \\ \quad + (\bar{x}_\xi \bar{y}_\eta - \bar{y}_\xi \bar{x}_\eta)(n_{25})_\zeta \\ (\bar{y}_\xi \bar{z}_\eta - \bar{z}_\xi \bar{y}_\eta)(n_{23})_\zeta + (\bar{x}_\eta \bar{z}_\xi - \bar{x}_\xi \bar{z}_\eta)(n_{25})_\zeta \\ \quad + (\bar{x}_\xi \bar{y}_\eta - \bar{y}_\xi \bar{x}_\eta)(n_{26})_\zeta \\ (\bar{y}_\xi \bar{z}_\eta - \bar{z}_\xi \bar{y}_\eta)(\bar{u}n_{21} + \bar{v}n_{22} + \bar{w}n_{23} + n_{27})_\zeta \\ \quad + (\bar{x}_\eta \bar{z}_\xi - \bar{x}_\xi \bar{z}_\eta)(\bar{u}n_{22} + \bar{v}n_{24} + \bar{w}n_{25} + n_{28})_\zeta \\ \quad + (\bar{x}_\xi \bar{y}_\eta - \bar{y}_\xi \bar{x}_\eta)(\bar{u}n_{23} + \bar{v}n_{25} + \bar{w}n_{26} + n_{29})_\zeta \end{bmatrix} \tag{3h}$$

$$n_{ij} = \sigma_{il}\ell_j + \sigma_{im}m_j, \quad i = 1,2, \quad j = 1,9 \tag{3i}$$

$$\begin{aligned}
\ell_1 &= \tfrac{2}{3}\bar{\mu}_{\text{eff}}(2\zeta_{\bar{x}}\bar{u}_\zeta - \zeta_{\bar{y}}\bar{v}_\zeta - \zeta_{\bar{z}}\bar{w}_\zeta) \\
\ell_2 &= \bar{\mu}_{\text{eff}}(\zeta_{\bar{y}}\bar{u}_\zeta + \zeta_{\bar{x}}\bar{v}_\zeta) \\
\ell_3 &= \bar{\mu}_{\text{eff}}(\zeta_{\bar{z}}\bar{u}_\zeta - \zeta_{\bar{x}}\bar{w}_\zeta) \\
\ell_4 &= \tfrac{2}{3}\bar{\mu}_{\text{eff}}(2\zeta_{\bar{y}}\bar{v}_\zeta - \zeta_{\bar{x}}\bar{u}_\zeta - \zeta_{\bar{z}}\bar{w}_\zeta) \\
\ell_5 &= \bar{\mu}_{\text{eff}}(\zeta_{\bar{y}}\bar{w}_\zeta + \zeta_{\bar{z}}\bar{v}_\zeta) \\
\ell_6 &= \tfrac{2}{3}\bar{\mu}_{\text{eff}}(2\zeta_{\bar{z}}\bar{w}_\zeta - \zeta_{\bar{x}}\bar{u}_\zeta - \zeta_{\bar{y}}\bar{v}_\zeta) \\
\ell_7 &= [\gamma\bar{k}_{\text{eff}}/(\gamma - 1)Pr]\,\zeta_{\bar{x}}(\bar{p}/\bar{\rho})_\zeta \\
\ell_8 &= [\gamma\bar{k}_{\text{eff}}/(\gamma - 1)Pr]\,\zeta_{\bar{y}}(\bar{p}/\bar{\rho})_\zeta \\
\ell_9 &= [\gamma\bar{k}_{\text{eff}}/(\gamma - 1)Pr]\,\zeta_{\bar{z}}(\bar{p}/\bar{\rho})_\zeta
\end{aligned} \tag{3j}$$

$$\begin{aligned}
m_1 &= \tfrac{2}{3}\bar{\mu}_{\text{eff}}(2\eta_{\bar{x}}\bar{u}_\eta - \eta_{\bar{y}}\bar{v}_\eta - \eta_{\bar{z}}\bar{w}_\eta) \\
m_2 &= \bar{\mu}_{\text{eff}}(\eta_{\bar{y}}\bar{u}_\eta + \eta_{\bar{x}}\bar{v}_\eta) \\
m_3 &= \bar{\mu}_{\text{eff}}(\eta_{\bar{z}}\bar{u}_\eta + \eta_{\bar{x}}\bar{w}_\eta) \\
m_4 &= \tfrac{2}{3}\bar{\mu}_{\text{eff}}(2\eta_{\bar{y}}\bar{v}_\eta - \eta_{\bar{x}}\bar{u}_\eta - \eta_{\bar{z}}\bar{w}_\eta) \\
m_5 &= \bar{\mu}_{\text{eff}}(\eta_{\bar{y}}\bar{w}_\eta + \eta_{\bar{z}}\bar{v}_\eta) \\
m_6 &= \tfrac{2}{3}\bar{\mu}_{\text{eff}}(2\eta_{\bar{z}}\bar{w}_\eta - \eta_{\bar{x}}\bar{u}_\eta - \eta_{\bar{y}}\bar{v}_\eta) \\
m_7 &= [\gamma\bar{k}_{\text{eff}}/(\gamma - 1)Pr]\eta_{\bar{x}}\,(\bar{p}/\bar{\rho})_\eta \\
m_8 &= [\gamma\bar{k}_{\text{eff}}/(\gamma - 1)Pr]\eta_{\bar{y}}\,(\bar{p}/\bar{\rho})_\eta \\
m_9 &= [\gamma\bar{k}_{\text{eff}}/(\gamma - 1)Pr]\eta_{\bar{z}}\,(\bar{p}/\bar{\rho})_\eta
\end{aligned} \tag{3k}$$

In Eqs. (1a) and (1b), μ_ℓ and k_ℓ are assumed to vary with temperature according to the empirical relations of Worsoe-Schmidt and Leppert,[9] as

$$\bar{\mu}_\ell = (\bar{p}/\bar{\rho})^{0.67} \tag{4a}$$

$$\bar{k}_\ell = (\bar{p}/\bar{\rho})^{0.71} \tag{4b}$$

The approximation to the Navier-Stokes equations employed in a particular calculation is controlled by the values of $\sigma_{i\ell}$ and σ_{im}. Generally, the η direction is normal to the wing and the ζ direction is normal to the fuselage. Euler calculations are performed over the wing surface when $\sigma_{1\ell} = \sigma_{1m} = 0$, thin-layer

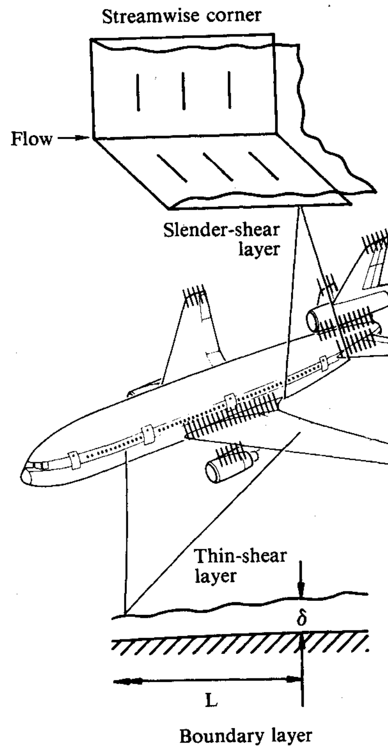

Fig. 1 Thin layers and slender layers (shaded areas) on a commercial transport plane in a cruise condition.

wing calculations when $\sigma_{1\ell} = 0$ and $\sigma_{1m} = 1$, and slender-layer wing calculations when $\sigma_{1\ell} = \sigma_{1m} = 1$. Similarly, Euler calculations are performed over the fuselage surface when $\sigma_{2\ell} = \sigma_{2m} = 0$, thin-layer fuselage calculations when $\sigma_{2\ell} = 1$ and $\sigma_{2m} = 0$, and slender-layer fuselage calculations when $\sigma_{2\ell} = \sigma_{2m} = 1$.

Turbulence Model

The Baldwin-Lomax algebraic turbulent eddy viscosity model[10] is employed to describe the effects of turbulence that enter through μ_t and k_t in Eqs. (1). In the slender-layer approximation, where there are viscous effects normal to two surfaces, the turbulent eddy viscosity at each point in the field is calculated relative to the closest surface.

The Baldwin-Lomax model is composed of two parts: one for the inner region and one for the outer region. In the inner region, the eddy viscosity is given by

$$(\bar{\mu}_t)_i = \bar{\rho}(K\bar{S}D)^2 \, |\bar{\omega}| \, (Re_\infty / \sqrt{\gamma} M_\infty) \tag{5}$$

where $K = 0.40$, $\bar{S}$ is the normal distance from the wall, and $|\bar{\omega}|$ the magnitude of the vorticity. The Van Driest damping factor D is given by

$$D = 1 - \exp(-S^+/A^+) \tag{6}$$

where

$$A^+ = 26$$

$$S^+ = \left(\frac{Re_\infty}{\sqrt{\gamma} M_\infty} \bar{\rho}_w \tau_w \right)^{\frac{1}{2}} \frac{\bar{S}}{(\bar{\mu}_{\text{eff}})_w} \tag{7}$$

$$\tau_w = (\mu_{\text{eff}})_w \frac{\partial u}{\partial n}\bigg|_w = (\bar{\mu}_{\text{eff}})_w \frac{\partial \bar{u}}{\partial n}\bigg|_w \frac{\rho_\infty U_\infty^2}{\sqrt{\gamma} Re_\infty M_\infty}$$

$$= \frac{c_f \rho_\infty U_\infty^2}{2} \tag{8}$$

Subscript w indicates values at the wall and n the direction normal to the wall. In regions where the flow separates, the wall shear stress becomes negative. Rather than use the absolute value of τ_w in Eq. (7), we use the τ_w value at the last station prior to separation throughout any separated region, thus eliminating any difficulty with τ_w being zero.

In the outer region, the eddy viscosity is determined by

$$(\bar{\mu}_t)_0 = 0.2688 \, \bar{\rho} F_{\text{wake}} F_{\text{kleb}} (Re_\infty / \sqrt{\gamma} M_\infty) \tag{9}$$

where

$$F_{\text{kleb}} = [1 + 5.5 \, (0.3 \, \bar{S}/\bar{S}_{\max})^6]^{-1} \tag{10}$$

The outer function F_{wake} is given by

$$F_{\text{wake}} = \min\left(\bar{S}_{\max} F_{\max}, \, 0.25 \frac{\bar{S}_{\max}}{F_{\max}} \bar{q}_{\max}^2 \right) \tag{11}$$

where

$$\bar{q}_{\max}^2 = \max(\bar{u}^2 + \bar{v}^2 + \bar{w}^2) \tag{12}$$

$$F_{\max} = \max(\bar{S} |\bar{\omega}| D) \tag{13}$$

and $\bar{S}_{\max}$ is the value of $\bar{S}$ at which $F_{\max}$ occurs.

The turbulent eddy viscosity is taken to be $(\bar{\mu}_t)_i$ from the surface to the point where $(\bar{\mu}_t)_0 \leq (\bar{\mu}_t)_i$. From that point outward, $\bar{\mu}_t = (\bar{\mu}_t)_0$. A wake turbulence model has not been included in the current algorithm.

Numerical Solution Procedure

The governing Eq. (2) is solved by an explicit, fourth-order Runge-Kutta time-marching finite-volume numerical scheme. The salient features of this procedure are outlined below.

Finite-Volume Method

The spatial and temporal terms in Eq. (2) are decoupled using the method of lines. The spatial computational domain is divided into hexahedral cells and a system of ordinary differential equations in time is obtained by integrating over each cell volume. The locations of the nodes at which the flowfield variables are calculated are the centers of cells formed by the grid points. A typical cell is shown in Fig. 2 where the node point (i,j,k) is surrounded by the six cell faces.

Integration of Eq. (2) over a cell of volume Ω and bounding surface $\partial\Omega$ gives

$$\iiint_\Omega \frac{\partial \hat{q}}{\partial \bar{t}} \, d\Omega + \iiint_\Omega \left(\frac{\partial \hat{L}}{\partial \bar{\xi}} + \frac{\partial \hat{M}}{\partial \bar{\eta}} + \frac{\partial \hat{N}}{\partial \bar{\zeta}} \right) d\Omega$$

$$= \frac{\sqrt{\gamma} M_\infty}{Re_\infty} \iiint_\Omega (\hat{S}_1 + \hat{S}_2) \, d\Omega \tag{14}$$

Let the values of the quantities associated with each cell (the average values for the cell at the cell center) be identified by the subscripts (i,j,k). Then, using Green's theorem to transform the second volume integral to a surface integral for each cell (i,j,k), Eq. (14) can be written in discretized form as

$$\frac{d}{dt}(J_{ijk} \hat{q}_{ijk}) + \hat{L}_{i+\frac{1}{2},j,k} - \hat{L}_{i-\frac{1}{2},j,k} + \hat{M}_{i,j+\frac{1}{2},k} - \hat{M}_{i,j-\frac{1}{2},k}$$

$$+ \hat{N}_{i,j,k+\frac{1}{2}} - \hat{N}_{i,j,k-\frac{1}{2}} = \frac{\sqrt{\gamma} M_\infty}{Re_\infty} J_{ijk} (\hat{S}_1 + \hat{S}_2)_{ijk} \tag{15}$$

Equation (15) is of the form

$$\frac{d}{dt}(J_{ijk} \hat{q}_{ijk}) + \mathfrak{F}_{ijk} = 0 \tag{16}$$

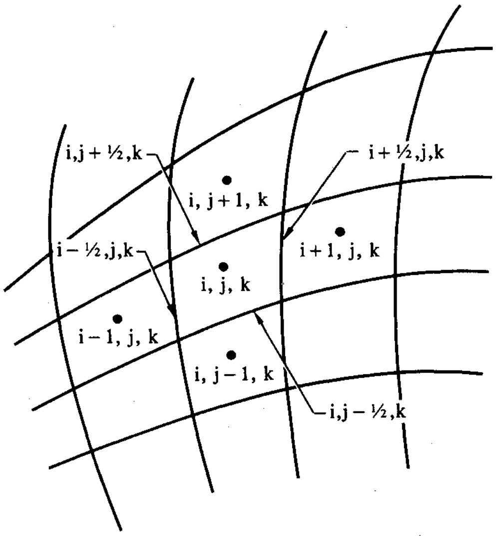

Fig. 2a Division of the computational domain into hexahedral cells (sketched on the k surface).

Fig. 2b A hexahedral cell in the physical domain.

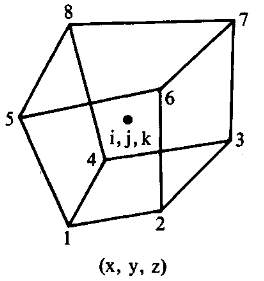

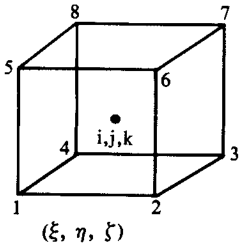

Fig. 2c The corresponding unit cube in the computational domain.

where the operator $\mathfrak{F}$ represents all the convective and viscous terms.

Dissipative Terms

To suppress the tendency for odd- and even-point decoupling and to prevent the appearance of oscillations in regions containing severe pressure gradients near shock waves and stagnation points, the finite-volume scheme must be augmented by the addition of artificial dissipative terms. Therefore, Eq. (16) is replaced by

$$\frac{\mathrm{d}}{\mathrm{d}t}(J_{ijk}\hat{q}_{ijk}) + \mathfrak{F}_{ijk} - D_{ijk} = 0 \tag{17}$$

where D_{ijk} denotes the dissipative terms. Jameson et al.[11] have established that an effective form of dissipative terms for flows with discontinuities is a blend of second and fourth differences with coefficients that depend on the local pressure gradient. Dissipative terms are constructed as follows:

$$D_{ijk} = (D_x + D_y + D_z)\hat{q}_{ijk} \tag{18}$$

where

$$D_x\hat{q}_{ijk} = d_{i+½,j,k} - d_{i-½,j,k} \tag{19}$$

The dissipative flux $d_{i+½,j,k}$ is defined as

$$d_{i+½,j,k} = \frac{J_{i+½,j,k}}{(\Delta\bar{t}_\ell)_{i+½,j,k}}\left(\epsilon^{(2)}_{i+½,j,k}\Delta_x\hat{q}_{ijk} - \epsilon^{(4)}_{i+½,j,k}\Delta^3_x\hat{q}_{i-1,j,k}\right) \tag{20}$$

where $\Delta_x\hat{q}_{ijk} = (\hat{q}_{i+1,j,k} - \hat{q}_{ijk})$, and $\epsilon^{(2)}$ and $\epsilon^{(4)}$ are adaptive coefficients defined below. We define

$$\nu_{ijk} = \left|\frac{\bar{p}_{i+1,j,k} - 2\bar{p}_{ijk} + \bar{p}_{i-1,j,k}}{\bar{p}_{i+1,j,k} + 2\bar{p}_{ijk} + \bar{p}_{i-1,j,k}}\right| \tag{21}$$

$$\epsilon^{(2)}_{i+½,j,k} = \kappa^{(2)}\max(\nu_{i+1,j,k}, \nu_{ijk}) \tag{22}$$

$$\epsilon^{(4)}_{i+½,j,k} = \max[0, (\kappa^{(4)} - \epsilon^{(2)}_{i+½,j,k})] \tag{23}$$

Typical values of the constants $\kappa^{(2)}$ and $\kappa^{(4)}$ are $\kappa^{(2)} = ¼$, $\kappa^{(4)} = 1/256$, and $(\Delta\hat{t}_\ell)_{ijk}$ is the local time step. The terms $D_y\hat{q}_{ijk}$ and $D_z\hat{q}_{ijk}$ in Eq. (18) are calculated in an analogous manner.

The scaling $J/\Delta\bar{t}$ in Eq. (20) conforms to the inclusion of the cell volume in the dependent variables of Eq. (17). Since Eq. (20) contains undivided differences, it follows that if $\epsilon^{(2)} = O(\Delta_x^{-2})$ and $\epsilon^{(4)} = O(1)$, then the added terms are of $O(\Delta_x^{-3})$, as will be the case in the regions where the flow is smooth. Near a shock wave, $\epsilon^{(2)} = O(1)$ and the scheme behaves locally as a first-order-accurate scheme.

Time-Stepping Scheme

The classical fourth-order Runge-Kutta scheme is used to integrate Eq. (17). Suppressing the subscripts (i,j,k), Eq. (17) can be written as

$$\frac{\mathrm{d}\hat{q}}{\mathrm{d}t} + \frac{1}{J}[\mathfrak{F}(\hat{q}) - D(\hat{q})] = 0 \tag{24}$$

At time level n, set

$$\hat{q}^{(0)} = \hat{q}^{(n)}$$

$$\hat{q}^{(1)} = \hat{q}^{(0)} - \frac{\Delta\bar{t}}{4J}[\mathfrak{F}\hat{q}^{(0)} - D\hat{q}^{(0)}]$$

$$\hat{q}^{(2)} = \hat{q}^{(0)} - \frac{\Delta\bar{t}}{3J}[\mathfrak{F}\hat{q}^{(1)} - D\hat{q}^{(0)}]$$

$$\hat{q}^{(3)} = \hat{q}^{(0)} - \frac{\Delta\bar{t}}{2J}[\mathfrak{F}\hat{q}^{(2)} - D\hat{q}^{(0)}]$$

$$\hat{q}^{(4)} = \hat{q}^{(0)} - \frac{\Delta\bar{t}}{J}[\mathfrak{F}\hat{q}^{(3)} - D\hat{q}^{(0)}]$$

$$\hat{q}^{n+1} = \hat{q}^{(4)} \tag{25}$$

In Eq. (25), the dissipative and viscous terms are frozen at their values in the first stage, thus avoiding expensive computations in each stage. The scheme is fourth-order accurate in time and is stable in Euler mode for Courant numbers $\leq 2\sqrt{2}$. Inclusion of viscous terms decreases the stability limit; the Courant number for Navier-Stokes runs is usually 0.9. The method has the property that if $[\mathfrak{F}\hat{q}^n - D\hat{q}^n] = 0$, then $\hat{q}^{(1)} = \hat{q}^{(0)}$, and so on, so that $\hat{q}^{n+1} = \hat{q}^n$ and the steady-state solution is

$$\mathfrak{F}\hat{q}^n - D\hat{q}^n = 0$$

independent of the time step. Thus, a variable time $(\Delta\bar{t}_\ell)$ determined by the bound on the local Courant number can be used to accelerate convergence to steady state without altering the steady state. To obtain time-accurate calculations of unsteady flow phenomena, the allowable time step is the smallest one in the field.

Boundary Conditions

At a body surface, flow tangency is the appropriate boundary condition for the Euler equations. Because the grid is body conforming and a finite-volume method is employed, the pressure is the only variable required. This is calculated assuming $\partial\bar{p}/\partial n = 0$, where n is the direction normal to the wall.

Thin- and slender-layer calculations require a no-slip condition at a surface so that $\bar{u} = \bar{v} = \bar{w} = 0$. The pressure at the surface is calculated assuming $\partial \bar{p}/\partial n = 0$. All calculations reported here assume an adiabatic wall temperature condition of the form $\partial \bar{H}/\partial n = 0$.

The treatment of the far-field boundary condition is based on the introduction of Riemann invariants for a one-dimensional flow normal to the boundary.[12] Let subscripts ∞ and e denote far-field values and values extrapolated from the interior cells adjacent to the boundary and let V_n and a be the velocity component normal to the boundary and the speed of sound, respectively.

If the flow in the far field is subsonic, introduce fixed and extrapolated Riemann invariants

$$R_\infty = V_{n\infty} - [2a_\infty/(\gamma - 1)] \quad \text{and} \quad R_e = V_{ne} + [2a_e/(\gamma - 1)]$$

corresponding to incoming and outgoing waves. These invariants may be added and subtracted to obtain

$$V_n = ½(R_e + R_\infty) \quad \text{and} \quad a = ¼(\gamma - 1)(R_e - R_\infty)$$

where V_n and a are the actual normal velocity component and the speed of sound to be specified in the far field, respectively. At an outflow boundary, the tangential velocity component and entropy are extrapolated from the interior, while at an inflow boundary they are specified as having far-field values. These four quantities provide a complete definition of the flow at the boundary.

If the flow is supersonic in the far field, all the quantities are specified at an inflow boundary and they are all extrapolated from the interior at an outflow boundary.

Code Optimization and Microtasking

The code has been fully vectorized and microtasked to optimally utilize four processors of a Cray X-MP/48. Microtasking was achieved by employing various software tools as described by Booth and Misegades.[13]

Computed Examples

Calculations have been performed for three different configurations: the ONERA-M6 wing, a typical transport wing/body configuration, and a typical fighter wing/body configuration. Similar calculations were reported in Ref. 14. However, in Ref. 14 the Euler, thin- and slender-layer models for the same case were run on different machines. Because the machines had different memory capabilities, different grid sizes were used, making a just comparison of the models difficult. The results reported here use the same grid for Euler, thin- and slender-layer calculations on a particular configuration.

Experimental data for the configurations reported here are limited to wing surface pressure data. Unfortunately, no experimental data are available for drag coefficient, skin-friction distributions, or boundary-layer profiles that might give a better indication of the accuracy of the viscous calculations.

ONERA-M6 Wing

Flow conditions chosen for this wing are $M_\infty = 0.84$, $\alpha = 3.06$ deg, and $Re_c = 11.72 \times 10^6$.

This standard test case was run on a mesh that had 192 cells wrapped around the wing, 32 cells normal to the wing surface, and 36 cells in the spanwise direction. There were 136 cells on the wing surface in the wraparound direction and 24 on the wing surface in the spanwise direction. The value of $y^+ = (y\sqrt{\tau_w \rho})/\mu$ at the center of the first cell was approximately four, with about 10 cells in the boudary layer. The grid was constructed by stacking two-dimensional sectional grids along the wing span. The two-dimensional sectional grids were generated using the MDRL algebraic grid-generation code.

Figure 3 compares pressure distributions on the wing at five span stations as predicted using the Euler and thin-layer models. Agreement with experimental data[15] is good in the leading- and trailing-edge regions. Shock smearing is greater than desirable, but can be attributed to the size of the cells in the mid-chord region. Cell width is typically 2–3% of the chord in this area, with shocks being smeared over three or four cells. More grid points in the wraparound direction or a better distribution with less clustering in the leading- and trailing-edge regions would produce sharper shocks.

The thin-layer model produces a more accurate prediction of the wing pressure distribution than the Euler model. Shock strength is too large and shock position is too far downstream when the Euler model is used. The thin-layer model, which includes the effects of the boundary layer, captures shock location and strength more accurately.

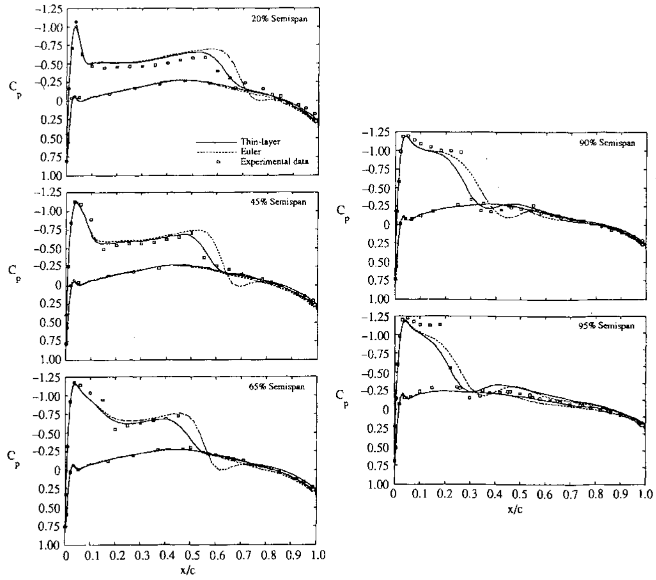

Fig. 3 Pressure distributions on an ONERA-M6 wing at various spanwise stations ($M_\infty = 0.84$, $\alpha = 3.06$ deg, $Re_c = 11.72 \times 10^6$, 192 × 32 × 36 mesh).

Table 1 Performance evaluation of the transonic viscous wing code on a Cray X-MP/48

- Test case: ONERA M6 wing
  $M_\infty = 0.84$, $\alpha = 3.06$ deg, $Re_c = 11.72 \times 10^6$
- Mesh used: 140 (chordwise) × 48 (wing-normal) × 32 (spanwise)
- Main memory required: 7.5 million words
- Processing rate on one processor: 2.3×10^{-5} CPU seconds/mesh point/iteration
- 98% of total CPU time spent in four key subroutines—EULER, FILTER, TSL1, EMUTURB
- Theoretical speedup on 4-processors (Amdahl's law):

$$\text{SP} = \frac{\text{CPU time}}{\text{wall clock time}} = \frac{1}{(0.98)/4 + (1 - 0.98)} = 3.77$$

- Actual speedup achieved after microtasking = 3.73
- Processing rate on 4-processors: 6.3×10^{-6} wall clock seconds/mesh point/iteration
- Total CPU time of microtasked code is 5% less than original code
- Number of iterations $N = 2500$
- Root-mean-square residual at $N = 1$ is 0.106×10^4
- Root-mean-square residual at $N = 2500$ is 0.4830
- Reduction/cycle = 0.997
- Total CPU time = 14400.00 s

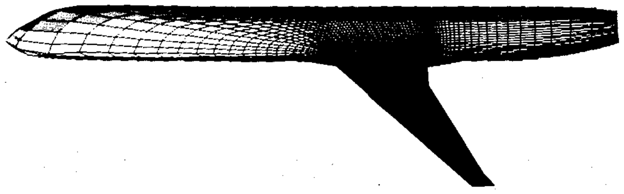

Fig. 4 Typical transport configuration with surface grid lines.

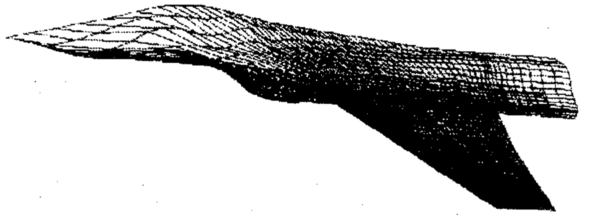

Fig. 7 Typical fighter configuration with surface grid lines.

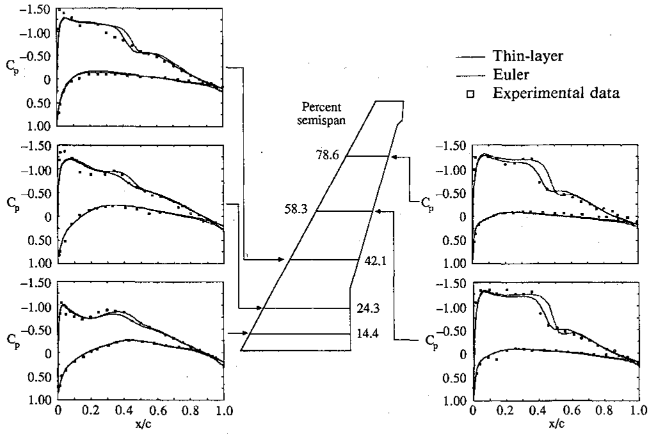

Fig. 5 Comparison of Euler and thin-layer Navier-Stokes pressure distributions with experimental data for a typical transport wing/body at $M_\infty = 0.76$, $Re_c = 6.39 \times 10^6$, $\alpha = 2.0$ deg, 160 × 34 × 42 mesh.

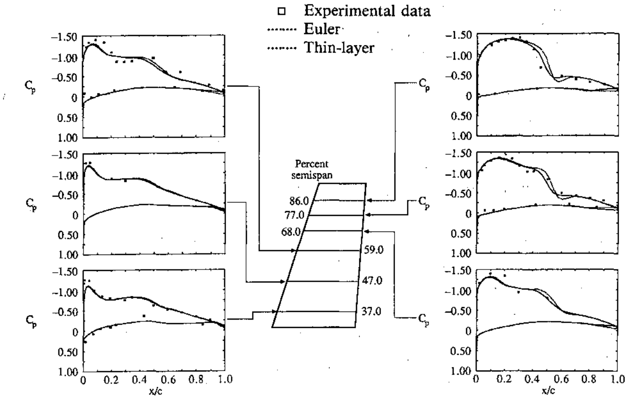

Fig. 8 Comparison of Euler and thin-layer Navier-Stokes pressure distributions with experimental data for a typical fighter aircraft wing/body at $M_\infty = 0.90$, $Re_c = 5.4 \times 10^6$, $\alpha = 4.8$ deg.

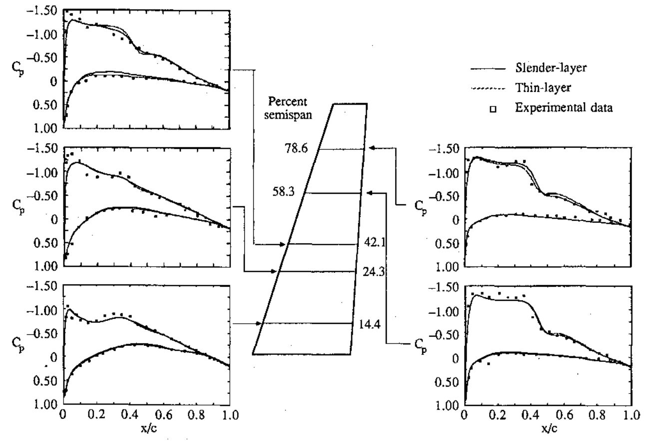

Fig. 6 Comparison of slender- and thin-layer Navier-Stokes pressure distributions with experimental data for a typical transport wing/body at $M_\infty = 0.76$, $Re_c = 6.39 \times 10^6$, $\alpha = 2.0$ deg, 160 × 34 × 42 mesh.

This case was also run on a smaller 140 × 48 × 32 grid on a four-processor machine to demonstrate the microtasking capability. The grid was limited by the eight-megaword capacity of the machine. Table 1 summarizes the results. Total run time using the microtasked version of the code was 1 h on each of the four available processors for a total CPU time of 4 h. The residuals dropped approximately 4 orders of magnitude in 2500 iterations at a Courant-Friedrichs-Levy (CFL) number of 0.9. The actual speedup in wall-clock time of 3.73 achieved by microtasking is very close to the theoretical maximum of 3.77 as determined by Amdahl's law.

Transport Wing/Body

The flow conditions chosen for this configuration are $M_\infty = 0.76$, $\alpha = 2$ deg, and $Re_c = 6.39 \times 10^6$.

A 160 (chordwise) × 34 (wing normal) × 42 (spanwise) mesh was generated with the three-dimensional code of Chen et al.[16] There are 96 cells on the wing in the chordwise direction and 34 in the spanwise direction. The value of y^+ at the center of the first cell along the wing surface ranges 1.5–3, while the value of y^+ at the center of the first cell along the fuselage surface varies 1.0–2.5. Figure 4 shows the grid lines on the surface.

Figure 5 shows the pressure distribution at five spanwise locations on the wing computed with the Euler and thin-layer Navier-Stokes codes, in comparison with experimental data. Thin-layer terms over the wing and the fuselage have been included in the calculations. As is the case with the ONERA-M6, the effect of including the thin-layer terms is to weaken shocks on the wing upper surface, move them forward, and improve the comparison with experimental data.

Figure 6 shows the slender-layer pressure distributions with thin-layer calculations in comparison with experimental data. As expected, there is little difference between the pressure distributions over the wing. The major effect of including slender-layer terms should be near the wing/fuselage junction. No experimental data are available for comparison in this region.

Fighter Wing/Body

Calculations were performed for a typical fighter wing/body configuration at $M_\infty = 0.9$, $\alpha = 4.84$ deg, and $Re_c = 5.4 \times 10^6$.

Again, the mesh was generated using the three-dimensional grid-generation code of Chen et al.[16] The grid has 144 cells in the chordwise direction, 34 cells normal to the wing, and 32 cells in the spanwise direction. Only the thin-layer terms near the wing have been included for this configuration, so there is no grid clustering near the fuselage to accommodate viscous effects. There are 96 cells on the wing surface in the chordwise direction and 24 in the spanwise direction. The value of y^+ at the center of first cell along the wing surface ranges 1.0–3.0. Figure 7 shows the grid lines on the surface.

Figure 8 shows the pressure distribution at five spanwise locations on the wing computed with the Euler and thin-layer

Navier-Stokes codes and their comparison with experimental data. Again, the viscous effects tend to weaken the wing upper-surface shocks and move them forward, although the effect is less pronounced for this configuration than for the transport wing/body discussed earlier.

Conclusions

A three-dimensional Navier-Stokes solver has been developed for viscous transonic flow about transport and fighter wing/body configurations. Calculations using Euler, thin- and slender-layer models are presented for flow about typical wing and wing/body configurations. Comparisons of calculated wing surface pressure distributions with experimental data show that thin-layer and slender-layer models yield better results for transonic flows. The Navier-Stokes methods predict shock strength and location more accurately than Euler calculations, which tend to place shocks too far downstream with greater strength than observed experi- mentally.

The code has been vectorized for efficient performance on vector processors and microtasked to optimally utilize multiple processors. On a four-processor machine, the ratio of CPU time to wall clock time is 3.73, very close to the theoretical limit of 3.77 determined from Amdahl's law.

Acknowledgments

This research was performed under the McDonnell Douglas Independent Research and Development program. The authors are grateful to M. Uram of McDonnell Douglas Aerospace Information Systems Company for programming assistance on Cray X-MP. They are also thankful to K. P. Misegades of Cray Research for microtasking the code on Cray X-MP/48 and providing the computational time.

References

[1] Agarwal, R. K. and Deese, J. E., "Computation of Viscous Airfoil, Inlet, and Wing Flowfields," AIAA Paper 84-1551, 1984.

[2] Agarwal, R. K., Deese, J. E., and Underwood, R. R., "Computation of Transonic Viscous Wing-Body Flowfields Using Unsteady Parabolized Navier-Stokes Equations," AIAA Paper 85-1595, 1985.

[3] Vatsa, V. N., "Accurate Solutions for Transonic Viscous Flow Over Finite Wings," AIAA Paper 86-1052, 1986.

[4] Holst, T. L. et al., "Numerical Solution of Transonic Wing Flows Using an Euler/Navier-Stokes Zonal Approach," AIAA Paper 85-1640, 1985.

[5] Vadyak, J., "Simulation of Diffuser Duct Flowfields Using a Three-Dimensional Euler/Navier-Stokes Algorithm" AIAA Paper 86-0310, 1986.

[6] Thomas, J. L. and Walters, R. W., "Upwind Relaxation Algorithm for the Navier-Stokes Equations," AIAA Paper 85-1501-CP, July 1985.

[7] Shang, J. S. and Scherr, S. J., "Navier-Stokes Solutions of the Flow-Field Around a Complete Aircraft," AIAA Paper 85-1509, 1985.

[8] Flores, J., Holst, T. L., Gundy, K. L., and Reznick, S. G., "Transonic Navier-Stokes Solutions for Fighter-Like Configurations," AIAA Paper 87-0032, Jan. 1987.

[9] Worsøe-Schmidt, P. M. and Leppert, G., "Heat Transfer and Friction for Laminar Flow of Gas in a Circular Tube at High Heating Rate," *International Journal of Heat and Mass Transfer,* Vol. 8, 1965, p. 1281.

[10] Baldwin, B. S. and Lomax, H., "Thin-Layer Approximation and Algebraic Model for Separated Turbulent Flows," AIAA Paper 78-257, 1978.

[11] Jameson, A., Schmidt, W., and Turkel, E., "Numerical Solutions of the Euler Equations by Finite Volume Methods Using Runge-Kutta Time-Stepping Schemes," AIAA Paper 81-1259, 1981.

[12] Jameson, A. and Baker, T. J., "Solution of the Euler Equations for Complex configurations," AIAA Paper 83-1929, 1983.

[13] Booth, M. and Misegades, K., "Microtasking: A New Way to Harness Multiprocessors," *Cray Channels,* Vol. 8, No. 2, Summer 1986, pp. 27–29.

[14] Deese, J. E. and Agarwal, R. K., "Navier-Stokes Calculations of Transonic Viscous Flow About Wing-Body Configurations," AIAA Paper 87-1200, 1987.

[15] Schmitt, V. and Charpis, F., "Pressure Distributions on the ONERA-M6-Wing at Transonic Mach Numbers," AGARD-AR-138, Chap. B-1.

[16] Chen, L. T., Vassberg, J. C., and Peavey, C. C., "A Transonic Wing-Body Flowfield Calculation with Improved Grid Topology and Shock-Point Operators," AIAA Paper 84-2157, 1984.